PAPER

Check for updates

^{19}F NMR as a tool to probe drug binding and structural dynamics in ferritin-based nanocarriers

Veronica Ghini,†[a] Giorgio Di Paco,†[a] Lucrezia Cosottini,[a] Antonio Rosato[ab] and Paola Turano ⓘ *[ab]

Ferritin-based nanocarriers offer a promising platform for targeted drug delivery due to their biocompatibility, stability, and ability to cross biological barriers. In this study, we used human heavy chain ferritin (HuHf) nanocage incorporating 5-fluorotryptophan to investigate the binding and structural dynamics of three gold(I)-based cytotoxic compounds: auranofin (AF), aurothiomalate (AuTM), and a gold(I)-N-heterocyclic carbene complex (AuNHC). Using ^{19}F NMR spectroscopy, we monitored site-specific interactions at the cysteine dyad (C90/C102) near the fluorinated tryptophan residue (W93), revealing distinct chemical shift signatures for each compound. Molecular dynamics simulations complemented the spectroscopic data, elucidating how conformational rearrangements of W93 correlate with the NMR shifts. Such rearrangements can change significantly the local environment of W93, affecting its solvent exposure as well as the distance from the gold(I) ion. These findings provide atomistic insight into the structural behavior of metallated ferritin nanocages and establish ^{19}F NMR as a powerful tool for probing protein–metal interactions in drug delivery systems also of nanoscale dimension.

Introduction

Nanoparticles used as drug delivery carriers consist of various materials such as synthetic polymers, lipids, metals, carbon and silica, possibly with capping agents such as chitosan, dextran and PEG. Several characteristics contribute to the production of a "good" nanocarrier, including particle size, shape and zeta potential. These properties affect cellular uptake, biodistribution and clearance.[1,2] An inherent problem is unwanted toxicity due to the nature of the nanomaterial used.[1,2]

The use of protein-based nanocarriers based on cage proteins (such as viral capsids, thermosomes, small heat shock proteins and ferritins) overcomes several of the above problems. Nanocage proteins have the advantage of uniform size and shape, remarkable stability, biocompatibility and biodegradability.[3] Among these, ferritin, and in particular human ferritin, stands out for its intrinsic targeting ability, low immunogenicity, high biocompatibility and biodegradability. It can cross the blood–brain barrier and selectively bind to specific receptors overexpressed in tumor cells, thereby enhancing targeted drug delivery.[4–6] As a result,

ferritin-based derivatives have been proposed for bioimaging and drug delivery (in addition to their use as nanoplatforms for vaccine development).[7,8] Active species can be loaded into ferritin by three main strategies: (i) free diffusion, for small charged entities (*e.g.* metal cations);[9,10] (ii) reversible disassembly of the cage followed by reassembly in the presence of the cargo molecules;[11,12] (iii) surface conjugation.[13–16] The latter approach is facilitated by the very large solvent-exposed surface ($>100\,000$ Å^2) of this hollow structure of 12 nm external diameter, which can be easily functionalized with native solvent-exposed amino acids.[17,18]

In our lab we have used homopolymers of recombinant human H ferritin (HuHf, hereafter) to target cancer cells over-expressing the transferrin receptor 1 (TfR1) with gold(I)-based cytotoxic compounds (*i.e.*, auranofin, AF; authiomalate, AuTM; gold-monocarbene, Au(NHC)Cl), Fig. 1.[13,14,19] The conjugation was achieved *via* stable coordination bonds with the thiolates of two solvent-exposed Cys residues (C90 and C102). Because they are located on the external cage surface and close to each other, they provide a cooperative binding site for the soft gold(I) ion. This cysteine-dyad is a unique feature of the cytoplasmic H-type ferritin compared with all the other types of human ferritin. Our previous studies have shown that conjugation of these compounds to ferritin produces highly cytotoxic species due to increased gold uptake.[13,14] However, the mechanism by which the active compound is released into the cell remains to be elucidated. Indeed, while release of encapsulated molecules is predominantly based on disassembly or degradation of the

[a] *Department of Chemistry "Ugo Schiff", University of Florence, 50019 Sesto Fiorentino, Italy. E-mail: paola.turano@unifi.it*

[b] *Magnetic Resonance Center (CERM), University of Florence, Sesto Fiorentino, FI, 50019, Italy*

† These authors contributed equally.
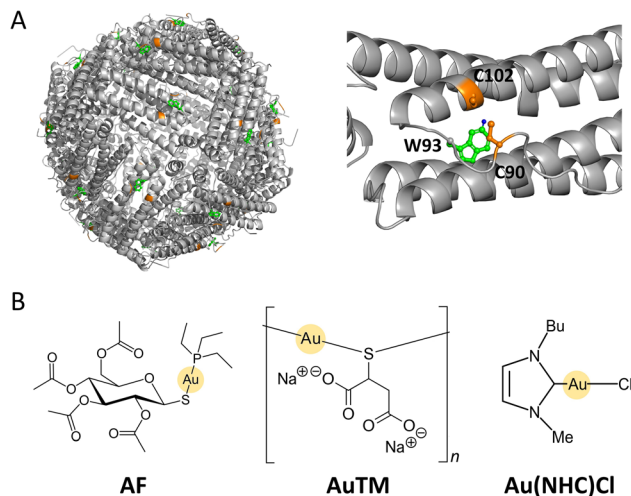
Fig. 1 (A) Structure of HuHf (PDB ID: 4Y08). Left panel: Outside view of the 24-mer nanocage with C90 and C102 highlighted in orange; W93 side chains are shown as green ball-and-stick representation. Right panel: close-up view of C90, C102 and W93 in a representative H subunit structure; ball-and-stick representation is used for cysteine side chains (orange) and tryptophan (green) with the ^{19}F at position 5 of the indole ring colored in blue. (B) Chemical structure of gold(I)-based cytotoxic compounds.

ferritin shell in the cellular environment, the factors affecting the cellular release of metal compounds coordinated on the external surface are less clear. It is reasonable to propose there is an interplay between affinity for HuHf and target intracellular proteins (such as thioredoxin reductase in the case of AF).[13,14,20]

To address this, we have designed a system that would allow us to monitor as well as discriminate between the free and metallated forms of HuHf simultaneously. To this end, we prepared a ^{19}F-labelled nanocage by selective fluorine incorporation into the side chain of W93, using 5-fluoroindole as the fluorinated precursor of this amino acid (Fig. 1A). Each ferritin subunit contains a single tryptophan, in close proximity to the two residues C90 and C102. Previous work showed that the ^{19}F chemical shift of this system changes upon binding a mercury(II)-compound to these cysteines.[21] Here we have used the same approach to monitor the binding of the aforementioned gold(I)-based cytotoxic compounds (Fig. 1B) and verified that the free and bound forms of HuHf can be clearly distinguished, in slow exchange on the ^{19}F chemical shift NMR time scale. Each compound caused peculiar chemical shift changes, which are interpreted in terms of rearrangements of the side chain of W93, as simulated by molecular dynamics calculations.

Results and discussion

The ^{19}F spectrum of the apo form of HuHf is shown in Fig. 2A. As previously reported,[21] it consists of a single peak centered at −124.85 ppm and with a linewidth of about 630 Hz. In contrast to our previous report,[21] this spectrum was obtained with a

new-generation spectrometer equipped with a 14.1 T magnet and a ^{19}F dedicated probe, which allowed a great increase in sensitivity. It should be noted that the use of magnetic field strengths of 11.7–14.1 T has been suggested as the best compromise between increased signal sensitivity and resolution and detrimental chemical shift anisotropy.[22] The acquisition time was reduced from 25 h with the old instrument down to 1 h at comparable sample concentration (5–15 μM ferritin cage) with the new spectrometer. The observation of a signal of reasonable linewidth in a nanocage protein of 506 kDa (in its fluorinated form) is not trivial. Indeed, the slow tumbling (and long rotational correlation time) of ferritin causes a significant signal broadening, which prevents detection in the case of most ^{1}H NMR signals.[23–25]

AF, AuTM and Au(NHC)Cl are three cytotoxic gold(I) compounds that have been characterized in our lab in terms of changes induced in the metabolome of ovarian cancer cells and found to affect different biochemical pathways.[14,26–28] Each of them is able to bind the ferritin surface *via* coordination bonds to C90 and C102, although with different stoichiometry and geometry. The three final adducts, *i.e.* those formed at the highest relative concentration of added compound, are hereafter referred to as HuHf@AF, HuHf@AuTM, and HuHf@AuNHC, following a convention used in our previous works.

AF (Fig. 1B, left) is a prodrug that binds proteins by losing its original thiosugar and retaining the triethylphosphine ligand; this activated gold(I)-phosphine form was proposed to bind HuHf by forming a "metal bridge" between the two thiolates of C90 and C120 on the same subunit, resulting in a trigonal arrangement (Fig. 3A). The maximum AF : HuHf cage ratio that could be obtained was ∼13, corresponding to about 50% of metallated subunits.[13] This is reflected in our NMR data, where the final ^{19}F spectrum still shows a non-negligible amount of apoprotein, while the signal attributable to the bound form resonates at −121.72 ppm and has a linewidth of the order of 820 Hz (Fig. 2B and C).

AuTM (Fig. 1B, middle) binds ferritin in the form of Au_3TM_2 units, with the two terminal gold(I) ions bound to C90 and C102 of the same subunit, respectively, and the central one bound to two thiomalates (Fig. 3B and C). With a molar excess of AuTM a fully metallated HuHf could be obtained, corresponding to approximately 70 gold ions per cage.[14] Accordingly, no appreciable apo signal is observed in the final NMR spectrum of HuHf with AuTM, (Fig. 2E). However, in contrast to the AF case, the bound form consists of two different species whose signals resonate at −122.85 and −116.75 ppm and have linewidths of about 1050 and 1400 Hz, respectively. The presence of two different forms has no counterpart in ESI MS spectra, which clearly indicates a single adduct (Fig. S1).[14] The relative ratio between the two forms is maintained in the spectra of Fig. 2D and E.

Au(NHC)Cl (Fig. 1B, right), under the active form of Au(NHC)$^+$ has high affinity for protein cysteines.[19,29] At variance with the other cases, where the structure of the adducts was modelled by MD starting from ESI MS and ICP-OES data, we were able to determine the high-resolution structure of the
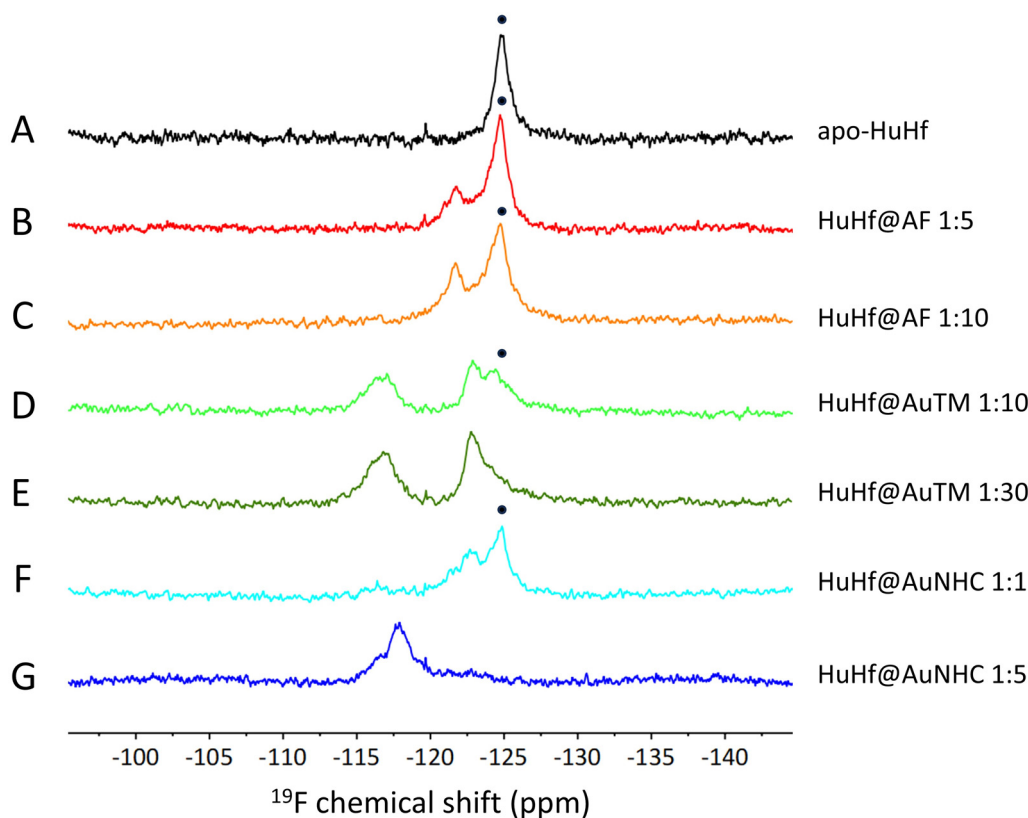
Fig. 2 ^{19}F NMR spectra of HuHf gold(I)-bioconjugates (15 μM) recorded at 14.1 T and 298 K; (A) apo-HuHf; (B) and (C) HuHf@AF; (D) and (E) HuHf@AuTM; (F) and (G) HuHf@AuNHC. ^{19}F chemical shifts were referenced to trifluoroacetic acid, used as an external standard (0 ppm). The ratios are given as subunit : compound, so, for example, a 1 : 10 ratio indicates that 10 equivalents of compound were added per ferritin subunit (i.e. per binding site), corresponding to 240 equivalents per cage. The black dot indicates the NMR signal of the apo form of the protein.

adduct containing 4 gold(I) ions bound to C90 and C102, in a zigzag arrangement and with relative distances consistent with the presence of aurophilic interactions (Fig. 3D).[19] In this case, we observed the appearance of two different bound forms: the first appears at halfway to the formation of the final adduct and features a resonance at −122.65 ppm with linewidth of about 1200 Hz (Fig. 2F); the second species, corresponding to the complete saturation, features a resonance at −117.77 ppm and linewidth of 1500 Hz (Fig. 2G).

The NMR spectra described above suggest different spectral properties of the final adducts, with the signal of the bound forms resonating at different chemical shifts. Nevertheless, by comparing the NMR spectra of Fig. 2, three different major groups of signals can be identified (i) the apo form, with the lowest shift (at ∼ −125 ppm) and a comparatively sharp line; (ii) the signals at ∼ −122 – 123 ppm for HuHf@AF, one of the two bound forms of HuHf@AuTM and the species formed when AuNHC is added in insufficient quantity to produce the fully bound form; (iii) the signals at ∼ −117 ppm for the second bound form of HuHf@AuTM and for saturated HuHf@AuNHC. It should also be noted that the resonances of the bound species are not simply broader than that of apo HuHf, but have a shape that suggests the presence of a complex envelope due to partially overlapping peaks, corresponding to multiple conformations in equilibrium. This is particularly evident for HuHf@AuNHC

(Fig. 2G), but also for HuHf@AuTM, especially when considering the fine structure of the cross peaks in Fig. 4. Indeed, the latter indicate not only that the two different gold-bound species of groups ii and iii are in conformational equilibrium with each other, but also that each signal actually contains two species in slow exchange. In other words, the EXSY spectrum demonstrates the existence of two pairs of interconverting conformations.

The chemical shift range of the signals in Fig. 2 is consistent with previous reports in the literature for proteins containing 5-fluorotryptophan.[30] In the present work we aim to provide an interpretation of the chemical shift perturbations observed for HuHf upon binding of the various gold(I) compounds. It has been reported that ^{19}F chemical shifts in proteins are sensitive to both electrostatic and van der Waals interactions with nearby atoms, in addition to the solvent effect.[31] Electrostatic effects would be expected to be important here because the formation of the HuHf adducts involves deprotonation of the Cys residues as well as the binding of charged ions to the site. However, the chemical shift changes observed upon amino acid substitution involving charged residues in the vicinity of buried tryptophans are <1 ppm.[32] Similarly, the use of a ^{19}F-labelled methyl group to monitor zinc(II) and cadmium(II) binding in a lactamase resulted in chemical shift variations of less than 1 ppm.[33]

Perturbations of similar magnitude have been reported for the binding of the charged organic m^{7}GpppG molecule to the
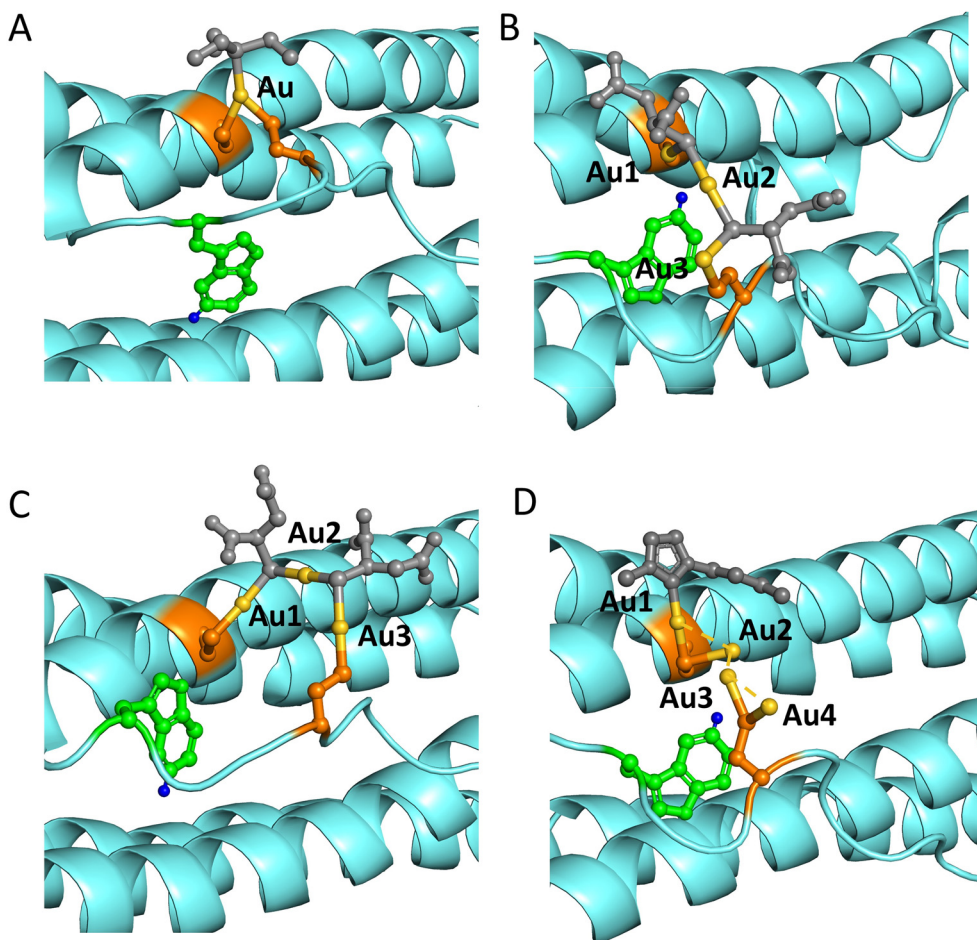
Fig. 3 Close-up view of the region of HuHf subunit containing C90, C102 and W93 in the different gold adducts. The structures of HuHf@AF (A) and HuHf@AuTM (B) and (C) have been obtained by a combination of modelling and MD calculations; that of HuHf@AuNHC (D) has been experimentally determined by cryo-EM (PDB id: 9HQ6). Panels B and C represent the two proposed orientations for W93 in the HuHf@AuTM adduct. In all panels the colour coding for the protein residues is the same as in Fig. 1A. Gold atoms are represented by yellow spheres and their non-protein ligands by grey ball-and-stick models.

DcpS scavenger decapping enzyme.[34] All these changes are significantly smaller than what observed here for the signals of group (iii) with respect to apo HuHf, namely up to 8 ppm (Fig. 2). We therefore hypothesized that the simple electrostatic effect due to the formation of the adduct could not justify our data. Thus, significant structural changes at and around W93 following metal binding should occur, at least for the species corresponding to the signals of group iii. This is a reasonable possibility given that W93 is bound to a long loop on the surface, where the packing of the structure is looser.

The shape and small linewidth (considering the large size of HuHf, with a correlation time for tumbling of the order of 130 ns)[24] of the ^{19}F signal in apo HuHf are consistent with the presence of a single conformation, or with multiple conformations interconverting in fast exchange on the NMR chemical shift time scale. The high-resolution X-ray crystal structure (PDB ID: 4Y08)[35] reveals a single well-defined orientation for W93 (see Fig. 1A, right panel). Starting from this structure, a 2-μs MD simulation of the apo HuHf cage showed that a change in the orientation of W93 is a rare event. Depending on the specific subunit analyzed, such reorientations could be associated either with a flip of the indole moiety (Fig. 5A), as indicated by the fact that only the χ_2 angle is affected (changing from +110°, Fig. 5B, to −70°, Fig. 5C), or, less commonly and with a very short lifetime, with a change in both χ_1 and χ_2 angles (not shown), indicating the sampling of an entirely different rotamer. Only in the former case, there was a systematic shortening of distance between the Sγ atoms of C90 and C102, upon transition from the initial conformation of the indole (observed in the static X-ray structure) to the transient one, corresponding to a change in the average distance from about 6.5 Å to about 4.5 Å (Fig. 5B and C). Such motions occurred on a time scale of hundreds of ns in the simulations (Fig. 5D).

We took the two extreme rotamers of W93, defined by the χ_1, χ_2 dihedral angle values of −50°, 100° (Fig. 5B) and of −60°, −90° as the starting structures for the modelling of the adducts HuHf@AF and HuHf@AuTM by MD simulations. In the case of HuHf@AF, for both starting structures the side chain reached a conformation with relatively constant χ_1 value oscillating
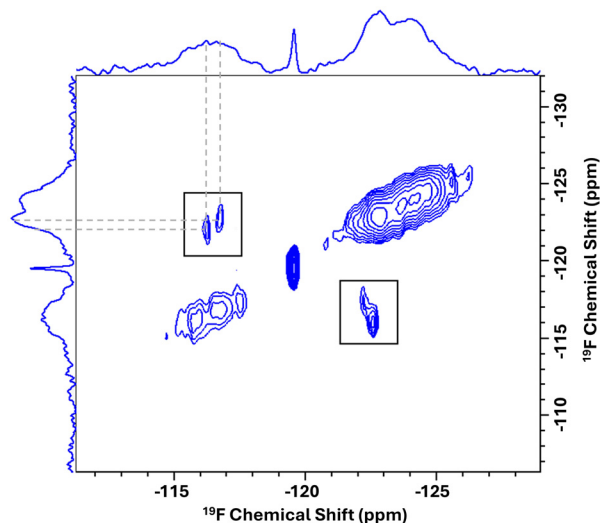
Fig. 4 ^{19}F–^{19}F EXSY spectrum of HuHf@AuTM 1:10 (subunit:compound) recorded at 298 K on a 14.1 T NMR spectrometer using a mixing time of 0.4 s; the corresponding 1D ^{19}F spectrum is reported both on the direct and indirect dimensions. Dashed lines indicate the components of the broad resonances of the 1D spectrum giving rise to exchange cross peaks. A lower threshold with respect to the diagonal was used for the boxed cross-peak analysis, to make them clearly visible.

around a mean value of about $-60°$ and positive but different χ_2 values ($+100°$ and $+50°$ respectively). At variance with the simulations for all other systems, the transition from the second starting structure featured also a rearrangement of the protein backbone in the W93 region, resulting in a relatively unique overall structure for W93 and its surroundings (Fig. 3A). For HuHf@AuTM we observed that the first conformation was maintained, although here the fluctuations of the χ_2 angle were larger than for HuHf@AF, whereas the simulation starting from the second structure experienced multiple transitions between positive and negative χ_2 angle values while χ_1 quickly took on negative values around $-80°$. Thus, in practice, W93 in HuHf@AuTM oscillated between two conformations depicted in Fig. 3B and C, respectively, which are quite similar to those of the apo HuHf depicted in Fig. 5B and C, respectively. In conformation 1 (Fig. 5B), which corresponds to the orientation observed in the crystal and cryo-EM structures of apo HuHf, the F atom in position 5 of the ring points towards the binding site of gold(I) ion, whereas in conformation 2 (Fig. 5C) position 5 points away from the site. The first spatial arrangement results in a F–Au distance of 5.5 Å, whereas the distance is 10 Å in the second spatial arrangement. The solvent accessibility of the F atom is about 26% larger in the first than in the second conformation, as computed on structures with gold(I) bound.

We are now in a position to correlate the NMR spectroscopy data with the structural data from experimental and MD studies to achieve an atom-level interpretation of the spectroscopic results. In HuHf@AF we observed the formation of only one species with ^{19}F chemical shift similar to that of the apo form (Fig. 2C). Instead, for HuHf@AuTM the NMR data at high gold(I) concentration indicated the presence of multiple species
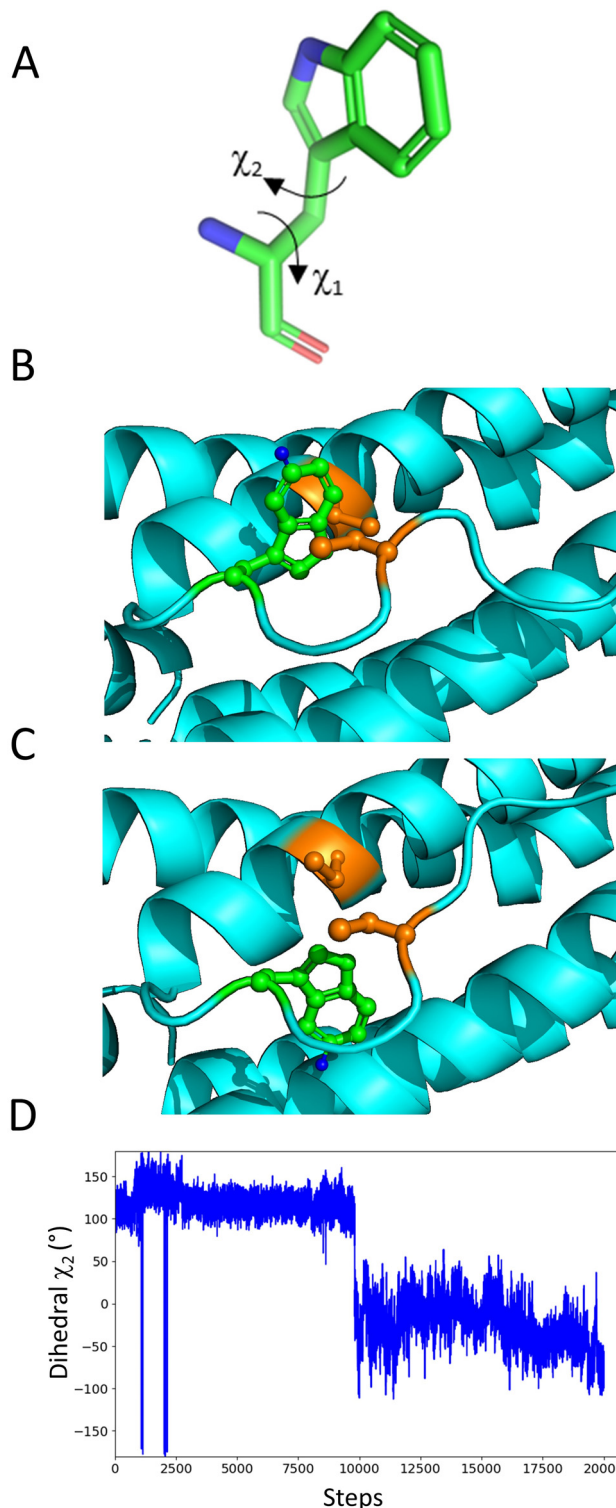
Fig. 5 (A) Dihedral angles denoted as χ_1 and χ_2 in tryptophan residues; (B) close-up view of W93 in the configuration with χ_1, χ_2 dihedral angle values of $-50°$, $100°$ sampled during the MD simulation of apo HuHf; (C) close-up view of W93 in the configuration with flipped ring, described by χ_1, χ_2 dihedral angle values of $-50°$, $-70°$; (D) variation of the χ_2 angle during the dynamics of apo HuHf when χ_1 remained at about $-50°$. The configuration of panel B corresponds to that of the crystal structure of apo HuHf.

(Fig. 2D and E), involved in conformational equilibria, as demonstrated by the presence of EXSY cross peaks in Fig. 4. Of these species, one group had a ^{19}F chemical shift similar to that of the apo form whereas the other had significantly smaller shift. Based on the MD data and the consideration on the determinants of ^{19}F chemical shift mentioned above, we can interpret the present data by assuming that the larger impact on shift is caused by the different environment and protein packing around the F atom in the sampled conformations.

Note that, based on the chemical shift separation among the signals and the detection of EXSY peaks, the experimental data point to an interconversion rate between the gold-bound species of the order of 10^2 s^{-1}.[36] This is much slower than what can be sampled with MD simulations. Hence, the different conformations of Fig. 3 and 5 can be regarded as examples of most frequent rearrangements sampled by MD, whereas even larger structural changes could take place in the system on longer time scales.

The ^{19}F chemical shift observed for apo HuHf is comparable to what reported in the literature for a solvent-exposed 5F-Trp side chain.[30] The fact that the chemical shift of the single NMR species in HuHf@AF (-121 ppm) was similar to that of the apo form (-124.8 ppm) suggests that the environment of the F atom is similar in the two systems. Fig. 3A–C shows that there can be multiple orientations of W93 and the loop containing it with respect to the rest of the subunit structure. For example, in the simulations of HuHf@AuTM two orientations of W93 have been detected that differ because of their F-gold(ı) distance (longest in Fig. 3C) and the solvent accessibility of the F atom (highest in Fig. 3C). Despite their large linewidths, the apo resonance and the envelope at -122.8 ppm undergo observable chemical shift changes upon H$_2$O/D$_2$O exchange (Fig. S2). This suggests that these species are more solvent accessible than those in the envelope at -116.7 ppm, although in the latter the changes may be more difficult to observe because of its even broader shape. It is also relevant that the presence of the gold(ı) ion and its organic ligands, such as the bulky phosphine in HuHf@AF, would make the F atom not accessible if the apo conformation was maintained. Thus, structural rearrangements are needed for the side chain of W93 to point away from the gold(ı) site and remain accessible (Fig. 3A).

Finally, the situation of HuHf@AuNHC is unique in the present series of compounds, as we detected that two distinct species formed with progressive addition of the metal compound. We previously demonstrated that this system formed different adducts at various protein : compound concentrations, in which the increasing concentration of gold(ı) triggers the onset of aurophilic interactions eventually leading to the formation of a tetra-gold cluster bound to the C90 and C103 residues.[19] Such interactions are fully formed at the HuHf@AuNHC ratio of Fig. 2G; thus, we can assume that the broad signal observed corresponds to the 3D arrangement observed in the cryoEM structure of the same system (PDB entry 9HQ6), shown in Fig. 3D, in which W93 maintains the conformation of the crystal structure. The tightly packed structure of the tetra-gold cluster causes a significant reduction of the solvent-exposure of the F atom in W93. Instead, at the 1 : 1 protein : AuNHC ratio of Fig. 2F,

the tetra-gold cluster is not yet formed, therefore the situation is akin to the HuHf@AF where W93 can rearrange.

Experimental

^{19}F HuHf preparation and characterization

The fluorinated human heavy chain ferritin (^{19}F HuHf) was expressed in M9 minimal medium in *E. coli* cells and purified as reported in a previous work published by our group.[21] 5-Fluoroindole, a precursor of 5-fluorotryptophan, was added to the medium and incubated for 15 min before the induction of ferritin overexpression with 1 mM IPTG, followed by an overnight growth at 25 °C.

Preparation of ^{19}F HuHf gold(ı) adducts

The reactions between ^{19}F HuHf and the three gold(ı) compounds *i.e.*, AF, AuTM and AuNHC were performed following the protocol described previously.[13,14] Briefly, the protein was incubated with increasing excess of the metal compounds in PBS, for 3 h at 37 °C; the excess was removed *via* several dialysis before the NMR experiments.

^{19}F NMR

All the NMR spectra were recorded at 298 K on a 14.1 T Bruker Advance NEO spectrometer, equipped with a QCI-^{19}F 5 mm probe. One dimensional NMR were obtained using a zg pulse sequence, with a recycle time of 3 s, an acquisition time of 0.57 s and a total number of scans of 8 k.

^{19}F–^{19}F EXSY experiment was performed on HuHf@AuTM 1 : 10 (subunit : compound) using a noesyph pulse sequence with 1024 points and spectral width of 50 ppm for the direct dimension, and 32 increments in the indirect dimension. 2 K scans per increment were acquired. A recycle delay of 2 s and a mixing time of 0.4 s were used.

Molecular dynamics

The X-ray structure of human H ferritin (PDB code: 4Y08) was used as the starting point of our investigation. The Chimera software[37] was employed to reconstruct the complete 24mer assembly. All the molecular dynamics simulations were performed with the pmemd software of the Amber23 suite.[38]

Three different scenarios were simulated: apo ferritin, ferritin in complex with auranofin (AF), and ferritin with aurothiomalate (AuTM). For each case, a specific MD simulation protocol was carried out, composed by 10 sequential steps in which the solvent and protein were minimized and equilibrated, ending with the production step. Overall, a total time of 2.0 µs for HuHf alone and 1.2 µs for each gold(ı)-containing system were simulated.

Each system was solvated in a 20 Å box of OPC water; the force fields used were protein.ff19SB for the ferritin 24-mer and gaff FF for the other molecules. The molecular parameters for AF and AuTM, like atomic charges, bond angles, dihedral angles, and bond distances, were derived from previous calculations for AuTm.[14] The same parameterization approach was applied to the AF molecule.

The solvent accessible surface was computed with the POPScomp server.[39]

Conclusions

This study demonstrates the usefulness of 5-fluorotryptophan as a sensitive probe for monitoring the binding of gold(I) compounds to the human ferritin nanocage *via* NMR spectroscopy. The distinct ^{19}F chemical shift signatures observed for the adducts formed by HuHf with AF, AuTM, and AuNHC reflect specific conformational rearrangements of the W93 side chain and its surroundings. The structural effects are influenced by the stoichiometry and geometry of the metal coordination as well as by the bulk of the gold(I) ligands. Molecular dynamics simulations provided atomistic insight into the features of different possible conformations, going from changes in rotameric state of the side chain to repositioning of the protein backbone in the loop of W93. This is the first time that we could monitor the effect on ^{19}F chemical shifts upon binding of a series of related gold(I)-compounds. The present work highlights the subtle effects of the different chemical coordination environments induced by the various gold(I) ligands onto the conformational equilibria within the nanocage.

The ability to detect distinct signals for HuHf when it is conjugated to metallodrugs bound in close proximity to W93 is important for future biological applications, such as detecting the intracellular release of drugs or studying competition binding experiments in solution. The general added value of ^{19}F lies in several aspects. Fluorinated amino acids can be easily incorporated into proteins using auxotrophic *E. coli* strains for protein expression or even simply by adding fluorinated precursors to the growth medium of regular *E. coli* cells. Additionally, fluorination can be achieved in different positions on aromatic rings. The insertion of ^{19}F into tryptophan residues has the advantage of providing site-selective information, given the low frequency of this amino acid in protein sequences (about 1% in the case of non-membrane proteins). The intrinsic mobility of the side chains renders the signals of ^{19}F visible even in very large macromolecules, such as protein nanocages.

The present findings underscore the potential of ^{19}F NMR as a powerful tool for characterizing metalloprotein interactions and for supporting the future development of ferritin-based nanocarriers for targeted drug delivery.

Author contributions

VG, GDP, LC: methodology; investigation. VG: writing – reviewing and editing. AR: data analysis; writing – original draft preparation. PT: data analysis; writing – original draft preparation; conceptualization/supervision.

Conflicts of interest

There are no conflicts to declare.

Data availability

This study was carried out using publicly available data from the Protein Data Bank at **https://www.ebi.ac.uk/pdbe/** with IDs 4Y08 and 9HQ6.

Materials and methods: electrospray mass spectrometry (ESI-MS), SDS-PAGE electrophoresis, analytical size exclusion chromatography, solvent-induced isotope effect experiments; SI Fig. S1 and S2. See DOI: **https://doi.org/10.1039/d5ma00538h**

References

1 M. J. Mitchell, M. M. Billingsley, R. M. Haley, M. E. Wechsler, N. A. Peppas and R. Langer, *Nat. Rev. Drug Discovery*, 2021, **20**, 101–124.
2 M. A. Beach, U. Nayanathara, Y. Gao, C. Zhang, Y. Xiong, Y. Wang and G. K. Such, *Chem. Rev.*, 2024, **124**, 5505–5616.
3 J. Kaltbeitzel and P. R. Wich, *Angew. Chem., Int. Ed.*, 2023, **62**, e202216097.
4 K. Fan, X. Jia, M. Zhou, K. Wang, J. Conde, J. He, J. Tian and X. Yan, *ACS Nano*, 2018, **12**, 4105–4115.
5 M. Liang, K. Fan, M. Zhou, D. Duan, J. Zheng, D. Yang, J. Feng and X. Yan, *Proc. Natl. Acad. Sci. U. S. A.*, 2014, **111**, 14900–14905.
6 Z. Wang, H. Gao, Y. Zhang, G. Liu, G. Niu and X. Chen, *Front. Chem. Sci. Eng.*, 2017, **11**, 633–646.
7 G. Jutz, P. van Rijn, B. Santos Miranda and A. Böker, *Chem. Rev.*, 2015, **115**, 1653–1701.
8 N. K. Lee, S. Cho and I.-S. Kim, *Exp. Mol. Med.*, 2022, **54**, 1652–1657.
9 T. Tosha, H.-L. Ng, O. Bhattasali, T. Alber and E. C. Theil, *J. Am. Chem. Soc.*, 2010, **132**, 14562–14569.
10 Y. Takezawa, P. Böckmann, N. Sugi, Z. Wang, S. Abe, T. Murakami, T. Hikage, G. Erker, Y. Watanabe, S. Kitagawa and T. Ueno, *Dalton Trans.*, 2011, **40**, 2190–2195.
11 L. Conti, S. Ciambellotti, G. E. Giacomazzo, V. Ghini, L. Cosottini, E. Puliti, M. Severi, E. Fratini, F. Cencetti, P. Bruni, B. Valtancoli, C. Giorgi and P. Turano, *Inorg. Chem. Front.*, 2022, **9**, 1070–1081.

12 N. Pontillo, F. Pane, L. Messori, A. Amoresano and A. Merlino, *Chem. Commun.*, 2016, **52**, 4136–4139.

13 L. Cosottini, L. Massai, V. Ghini, S. Zineddu, A. Geri, M. Mannelli, S. Ciambellotti, M. Severi, T. Gamberi, L. Messori and P. Turano, *J. Drug Delivery Sci. Technol.*, 2023, **87**, 104822.

14 L. Cosottini, A. Geri, V. Ghini, M. Mannelli, S. Zineddu, G. Di Paco, A. Giachetti, L. Massai, M. Severi, T. Gamberi, A. Rosato, P. Turano and L. Messori, *Angew. Chem., Int. Ed.*, 2024, e202410791.

15 M. Liu, Y. Zhu, T. Wu, J. Cheng and Y. Liu, *Chem. – Eur. J.*, 2020, **26**, 7442–7450.

16 J. Hong, K. Li, J. He and M. Liang, *Bioconjugate Chem.*, 2024, **35**, 1142–1147.

17 E. Ravera, S. Ciambellotti, L. Cerofolini, T. Martelli, T. Kozyreva, C. Bernacchioni, S. Giuntini, M. Fragai, P. Turano and C. Luchinat, *Angew. Chem., Int. Ed.*, 2016, **55**, 2446–2449.

18 M. Sengonul, J. Ruzicka, A. B. Attygalle and M. Libera, *Polymer*, 2007, **48**, 3632–3640.

19 L. Cosottini, A. Giachetti, A. Guerri, A. Martinez-Castillo, A. Geri, S. Zineddu, N. G. A. Abrescia, L. Messori, P. Turano and A. Rosato, *Angew. Chem., Int. Ed.*, 2025, e202503778.

20 A. Bindoli, M. P. Rigobello, G. Scutari, C. Gabbiani, A. Casini and L. Messori, *Coord. Chem. Rev.*, 2009, **253**, 1692–1707.

21 L. Cosottini, S. Zineddu, L. Massai, V. Ghini and P. Turano, *J. Inorg. Biochem.*, 2023, **244**, 112236.

22 C. T. Gee, K. E. Arntson, A. K. Urick, N. K. Mishra, L. M. L. Hawk, A. J. Wisniewski and W. C. K. Pomerantz, *Nat. Protoc.*, 2016, **11**, 1414–1427.

23 M. Matzapetakis, P. Turano, E. C. Theil and I. Bertini, *J. Biomol. NMR*, 2007, **38**, 237–242.

24 D. Lalli and P. Turano, *Acc. Chem. Res.*, 2013, **46**, 2676–2685.

25 P. Turano, D. Lalli, I. C. Felli, E. C. Theil and I. Bertini, *Proc. Natl. Acad. Sci. U. S. A.*, 2010, **107**, 545–550.

26 V. Ghini, T. Senzacqua, L. Massai, T. Gamberi, L. Messori and P. Turano, *Dalton Trans.*, 2021, **50**, 6349–6355.

27 V. Ghini, M. Mannelli, L. Massai, A. Geri, S. Zineddu, T. Gamberi, L. Messori and P. Turano, *RSC Adv.*, 2023, **13**, 21629–21632.

28 V. Ghini, A. I. Tristán, G. Di Paco, L. Massai, M. Mannelli, T. Gamberi, I. Fernández, A. Rosato, P. Turano and L. Messori, *J. Proteome Res.*, 2025, **24**, 813–823.

29 C. Zoppi, L. Massai, D. Cirri, C. Gabbiani, A. Pratesi and L. Messori, *Inorg. Chim. Acta*, 2021, **520**, 120297.

30 J. M. Aramini, K. Hamilton, L.-C. Ma, G. V. T. Swapna, P. G. Leonard, J. E. Ladbury, R. M. Krug and G. T. Montelione, *Structure*, 2014, **22**, 515–525.

31 M. A. Danielson and J. J. Falke, *Annu. Rev. Biophys. Biomol. Struct.*, 1996, **25**, 163–195.

32 M. Maxwell, Y. J. Tan, R. Lee, T. Huber and G. Otting, *Biochemistry*, 2023, **62**, 3255–3264.

33 A. M. Rydzik, J. Brem, S. A. Chandler, J. L. P. Benesch, T. D. W. Claridge and C. J. Schofield, *RSC Med. Chem.*, 2020, **11**, 387–391.

34 C. Krempl and R. Sprangers, *J. Biomol. NMR*, 2023, **77**, 55–67.

35 C. Pozzi, F. Di Pisa, C. Bernacchioni, S. Ciambellotti, P. Turano and S. Mangani, *Acta Crystallogr., Sect. D: Biol. Crystallogr.*, 2015, **71**, 1909–1920.

36 I. R. Kleckner and M. P. Foster, *Biochim. Biophys. Acta*, 2011, **1814**, 942–968.

37 E. C. Meng, T. D. Goddard, E. F. Pettersen, G. S. Couch, Z. J. Pearson, J. H. Morris and T. E. Ferrin, *Protein Sci.*, 2023, **32**, e4792.

38 D. A. Case, H. M. Aktulga, K. Belfon, D. S. Cerutti, G. A. Cisneros, V. W. D. Cruzeiro, N. Forouzesh, T. J. Giese, A. W. Götz, H. Gohlke, S. Izadi, K. Kasavajhala, M. C. Kaymak, E. King, T. Kurtzman, T.-S. Lee, P. Li, J. Liu, T. Luchko, R. Luo, M. Manathunga, M. R. Machado, H. M. Nguyen, K. A. O'Hearn, A. V. Onufriev, F. Pan, S. Pantano, R. Qi, A. Rahnamoun, A. Risheh, S. Schott-Verdugo, A. Shajan, J. Swails, J. Wang, H. Wei, X. Wu, Y. Wu, S. Zhang, S. Zhao, Q. Zhu, T. E. I. Cheatham, D. R. Roe, A. Roitberg, C. Simmerling, D. M. York, M. C. Nagan and K. M. Jr. Merz, *J. Chem. Inf. Model.*, 2023, **63**, 6183–6191.

39 J. Kleinjung and F. Fraternali, *Nucleic Acids Res.*, 2005, **33**, W342–W346.